

SUPPLEMENTARY MATERIAL

Effects of the charge-transfer reorganization energy on the open-circuit voltage
in small-molecular bilayer organic photovoltaic devices: comparison in
influences of donor deposition rate

Chih-Chien Lee*, Wei-Cheng Su, Wen-Chang-Chang

Department of Electronic Engineering, National Taiwan University of Science and
Technology, Taipei 10607, Taiwan

*Correspondence to clee@mail.nsut.edu.tw

S1. Device Configuration of the OPV Devices

Figure S1 shows the device configuration, energy-level diagram, and molecular structures of the materials used in the current study. The HOMO levels were estimated using a low-energy photoelectron spectrometer (Riken Keiki AC-2) [1, 2]. The LUMO levels were calculated by subtracting the HOMO by the optical band-gap obtained from a UV-vis spectrophotometer (Thermo Scientific Evolution 220).

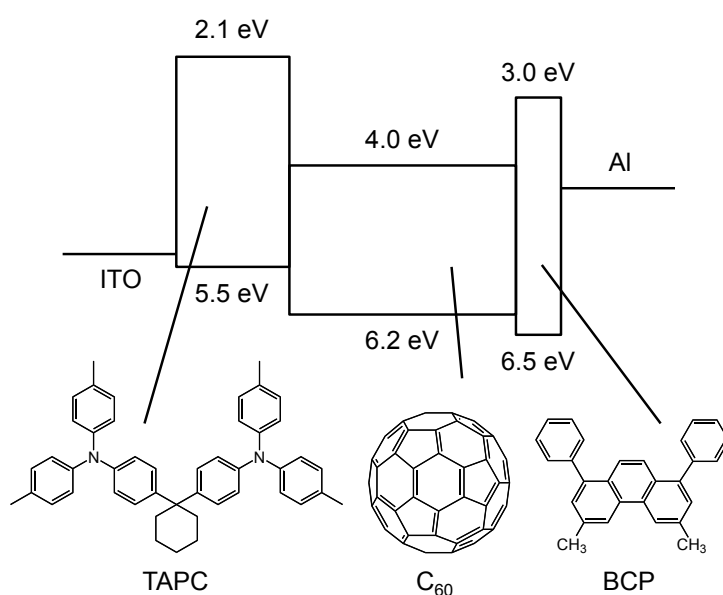


Figure S1. Device configuration, energy-level diagram, and molecular structures of the materials used in the current study.

S2. Variation of the Deposition Rates of the TAPC during the Deposition Process

Figure S2 shows the variation of various TAPC deposition rates. The deposition rate of each cell parameter was recorded per second. Errors of approximately 5.0%, 6.7%, and 11% were estimated for deposition rates of 0.03, 0.15, and 0.80 nm/s, respectively.

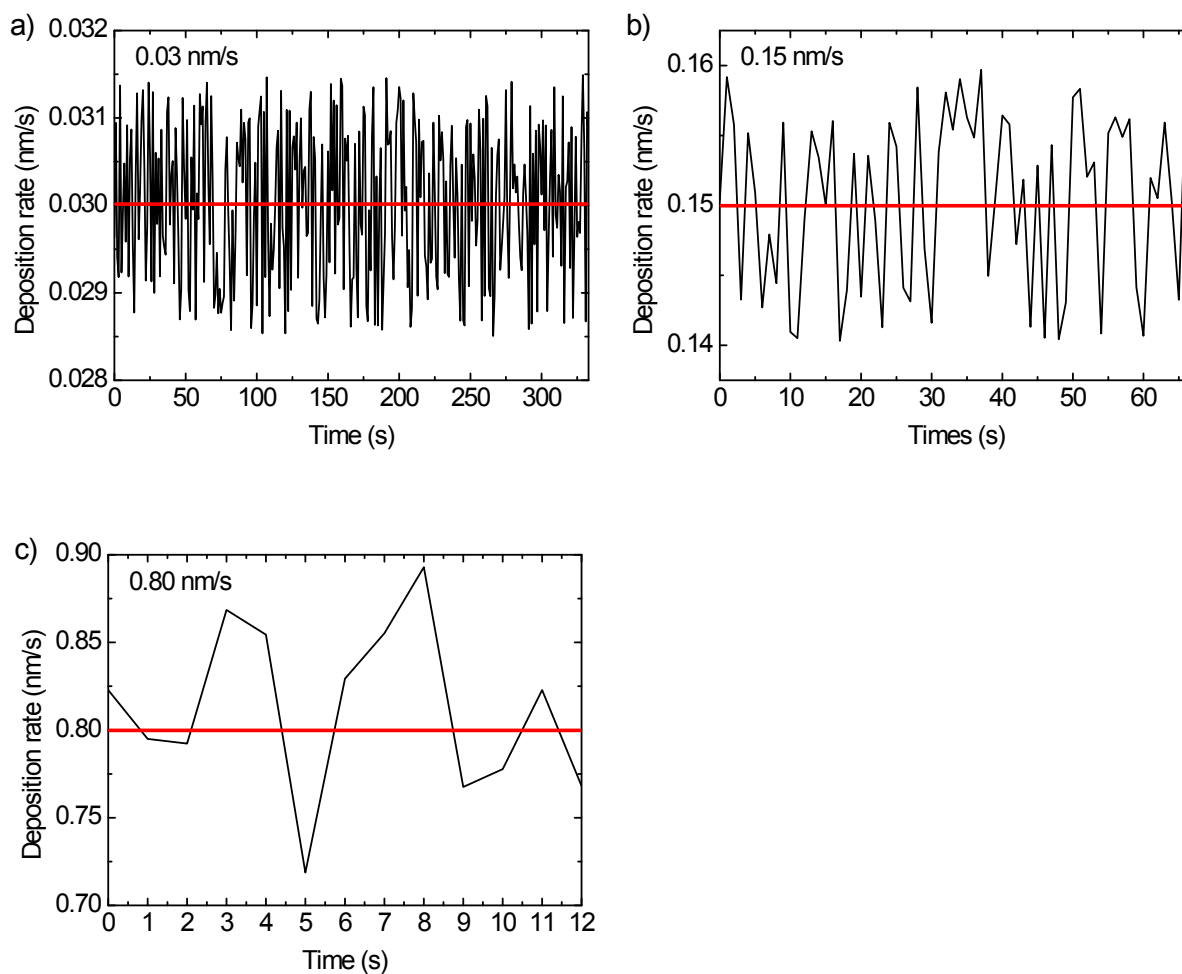


Figure S2. *In situ*, simultaneous monitoring of the variation of various TAPC deposition rates during the thin-film deposition. The red lines indicate the desirable deposition rates.

S3. Thickness-Dependent Test of the TAPC/C₆₀ OPV Devices

Figure S3 shows the photo and dark J - V characteristics of the device structure of ITO/TAPC (8, 10, 12, and 14 nm)/C₆₀ (40 nm)/BCP (10 nm)/Al with the TAPC deposited at 0.10 nm/s. The inset shows that the V_{OC} was the same for all the thicknesses, whereas a slight decrease in J_{SC} and FF was observed. Although the TAPC has a hole mobility in the order of approximately 10^{-2} cm² V⁻¹ s⁻¹ at high electric fields [3, 4], in OPV devices the electric field should be low. Therefore, when the thickness of TAPC was increased the carrier transport decreased, leading to the poor electrical properties. The forward current in the dark is consistent with this inference, because the dark current gradually decreased when the TAPC thickness was increased.

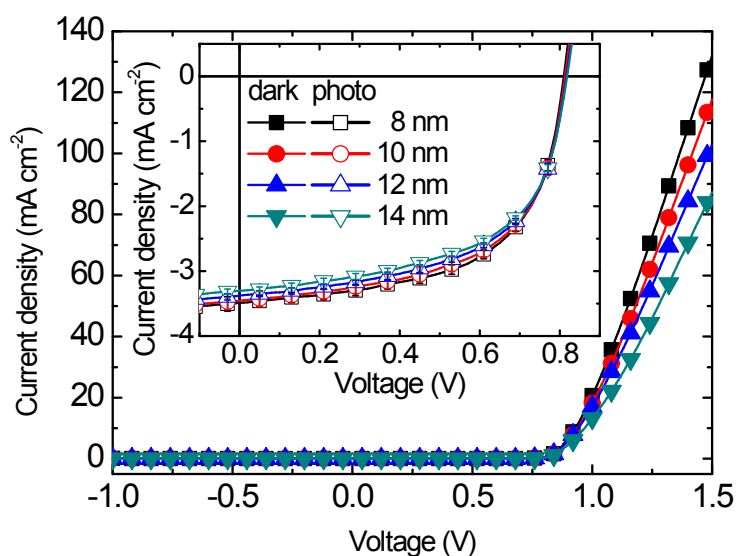


Figure S3. Photo and dark J - V characteristics of the device structure of ITO/TAPC (8, 10, 12, and 14 nm)/C₆₀ (40 nm)/BCP (10 nm)/Al with the TAPC deposited at 0.10 nm/s. The solid and open symbols denote the dark and photo currents, respectively.

S4. Influence of the Deposition Rates on the Electronic States of the TAPC

Figure S4a shows the estimation of the HOMO levels of 10-nm TAPC films deposited at various deposition rates. The onset points at high energy correspond to the HOMO levels of the TAPC according to the photoelectric effect; the lowest energy required for removing the electron on the sample surface when light shines on the surface. Figure 4b shows the absorbance of TAPC thin films. The onset points at a low-wavelength range (i.e., high-energy level) indicate an optical band-gap. Therefore, the LUMO levels can be calculated by subtracting the HOMO level from the optical band-gap. As shown in these figures, the HOMO and LUMO levels were maintained the same when the deposition rate of the TAPC was varied from 0.03 and 0.15 to 0.80 nm/s, thus indicating that the electronic states of the TAPC were not affected by the deposition rates.

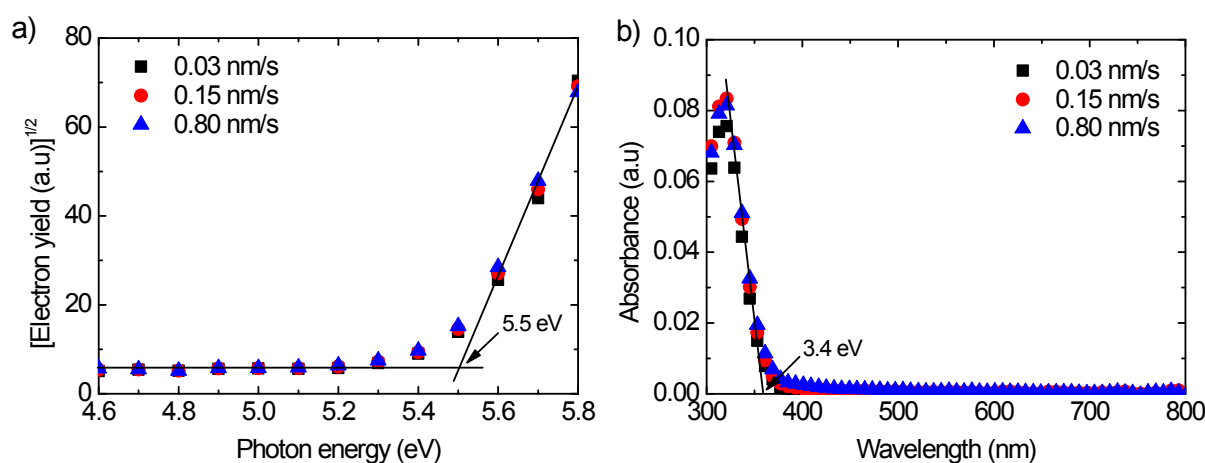


Figure S4. a) Low-energy photoelectron and b) UV-vis spectroscopic spectra for the 10-nm TAPC films deposited at various deposition rates.

S5. Extraction of the CT Properties from the CT absorption Band and the CT Emission

Equations (5) and (6) in the main text represent the CT absorption band and the CT emission rate, respectively. Both equations have a Gaussian-distribution form as shown in Equation (S1):

$$y = \frac{A}{w\sqrt{\frac{\pi}{2}}} \exp\left[-\frac{(x-x_c)^2}{\frac{w^2}{2}}\right] \quad (\text{S1})$$

The variable A is the maximum height of the Gaussian distribution, w is the Gaussian-distribution width, and x_c is the central position of the Gaussian distribution. The corresponding reduced spectra of the CT states can be obtained by replacing y with $\text{EQE}(E)E$ and I_f/E for the CT absorption and emission, respectively, A with f (or f_i), x with E , w with $\sqrt{8\lambda kT}$, and x_c with $(E_{\text{CT}} + \lambda)$ and $(E_{\text{CT}} - \lambda)$ for the CT absorption and emission, respectively. Thus, the fits of the reduced EQE and EL spectra to the Gaussian distribution yield the CT properties, f , E_{CT} , and λ , as shown in Table 2.

S6. Calculations of the Energetic Losses of the OPV Devices

Recall Equation (9) as Equation (S2):

$$V_{OC} = \frac{E_{CT}}{q} + \frac{kT}{q} \ln \left[\frac{J_{SC} h^3 c^2}{f q 2\pi (E_{CT} - \lambda)} \right] + \frac{kT}{q} \ln(\text{EQE}_{EL}) \quad (\text{S2})$$

Here, the V_{OC} was experimentally obtained. The f , E_{CT} , and λ , were obtained as described in Section S5. The first term on the right side in Equation (S2), which corresponds to the theoretical maximum of the V_{OC} , can be directly calculated by dividing E_{CT} by q , both of which are in a unit of eV. Before calculating the second term, we transformed the units of f and $(E_{CT} - \lambda)$ from eV to V, which yielded the cubic elementary charges, q^3 . Therefore, we first calculated $h^3 c^2 / q^4$, which equals approximately $3.968 \times 10^{-8} \text{ J}^3 \text{ m}^2 \text{ s C}^{-4}$. By substituting the experimental J_{SC} in a unit of A m^{-2} and the remaining parameters, the natural-logarithmic term can be obtained, thus yielding the values of the radiative energetic losses, ΔV_{rad} , as provided in Table 2. Because the experimental V_{OC} on the left side and the first and second terms on the right side were known, the third term in Equation (S2) was directly calculated, yielding the EQE_{EL} of the OPV devices and, hence, the nonradiative energetic losses ΔV_{nonrad} , as provided in Table 2.

S7. Morphological Change of the TAPC Thin Films on ITO Surface

Figure S5a-c shows the morphology (5 by 5 μm) of the TAPC deposited on an ITO surface with various deposition rates. Figure S5d-f shows the corresponding morphology over a smaller area (2 by 2 μm). The surface roughness is described in a text in the bottom-right corner for each image. The surface roughness of the pristine ITO was approximately 3.0 nm. At the lowest deposition (0.03 nm/s) the surface was blurred. When the deposition rate of the TAPC increased, the surface became clear, especially at the highest deposition rate (0.80 nm/s) and exhibited features of a pristine ITO surface. These results indicate that a higher deposition rate led to a decreased aggregation of the TAPC molecules.

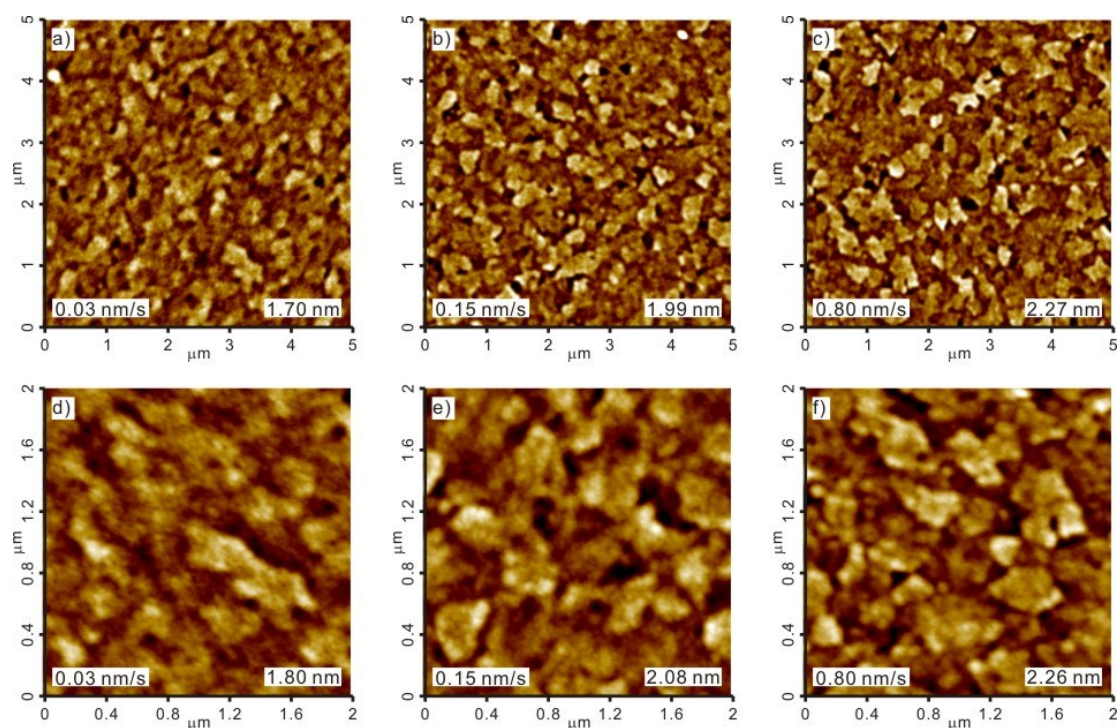


Figure S5. AFM images of 10-nm TAPC thin films deposited at various deposition rates on ITO substrates (roughness: 3.0 nm) over an area of a-c) 5 by 5 μm and d-f) 2 by 2 μm . The surface roughness of each thin film is provided in the bottom-right corner.

S8. Investigating the Electronic Properties of the TAPC Thin Films using a GDM and CGDM

Before using the GDM and CGDM, the temperature-dependent mobility μ of the hole-only devices with the TAPC deposited at various deposition rates was obtained to determine the zero-field mobility μ_0 and Poole-Frenkel factor β . The hole-only devices had a structure of ITO/MoO₃ (5 nm)/TAPC (100 nm)/MoO₃ (5 nm)/Al (120 nm) with the TAPC single layer deposited at various deposition rates. The ITO and Al electrode were positively and negatively biased, respectively. The space-charge limit current (SCLC) model without an electric-field dependence can be expressed in Equation (S3) [5, 6]:

$$J = \frac{9}{8} \varepsilon_r \varepsilon_0 \frac{E^2}{L} \mu \quad (\text{S3})$$

Here, ε_r and ε_0 are the relative dielectric constant and the permittivity of the free space, respectively, E is the electric field, L is the thickness of the material undergoing testing, and J is the current density of the devices, which was experimentally obtained by determining the J - V characteristics of the hole-only devices. The ε_r was determined using a precision LCR meter (Agilent 4980A), and the value was approximately 3.1 for all the devices. Figure 5a-c shows the SCLCs for the devices with the TAPC deposited at various deposition rates with varied temperatures. The experimental results (open symbols) were consistent with the fits according to the SCLC model. However, the carrier mobility μ exhibited a certain degree of electric-field dependence. Therefore, the SCLC model should account for the Poole-Frenkel effect, as shown in Equation (S4) [5, 6]:

$$J(E) = \frac{9}{8} \varepsilon_r \varepsilon_0 \frac{E^2}{L} \mu_0 \exp(\beta \sqrt{E}) \quad (\text{S4})$$

By plotting $\ln(J/E^2)$ against the square root of the electric field E , the Poole-Frenkel factor β can be extracted from the slope of the curve, as shown in Figure S6d-f. Thus, the zero-field mobility μ_0 can be obtained by substituting the E for zero, as shown in Figure S6g-i.

The carrier mobility in a lattice of localized states is typically affected by the fluctuation of energetic and positional disorders. The GDM estimates the energetic and positional disorders as proposed by Bäessler in Equation (S5) [7]:

$$\mu(T, E) = \mu_{\infty} \exp\left[-\left(\frac{2\sigma}{3kT}\right)^2\right] \exp\left\{C_0 \sqrt{E} \left[\left(\frac{\sigma}{kT}\right)^2 - \Sigma^2\right]\right\} \quad (\text{S5})$$

Here, μ_{∞} is a temperature-independent mobility prefactor, σ is the energetic disorder of the GDM, k is the Boltzmann constant, T is the temperature, C_0 is a constant that depends on the site-to-site distance of molecules, Σ^2 is the positional disorder of the GDM. First, by plotting $\mu(T, 0)$ as a function of $(1000/T^2)$, as shown in Figure S7a, the slope and intercept yielded the energetic disorder σ and mobility prefactor μ_{∞} of the GDM. The dependence of the Poole-Frenkel factor β on $(\sigma/kT)^2$ enabled extracting the constant C_0 and positional disorder Σ^2 of the GDM, as shown in Figure S7b. The results are summarized in Table S1. The μ_{∞} decreased when the deposition rate of the TAPC was increased; this may indicate a reduced electrical property, as inferred in the main text. A possible reason for the decreased electrical property may be the fluctuation of the σ , which exhibited an increasing trend that was related to the deposition rate. However, the Σ^2 was negative in the device with the TAPC deposited at 0.80 nm/s. The negative value in general has no physical meaning. Therefore, a more precise model, the CDGM, has been proposed or considering the spatially correlated energetic disorder in disordered organic materials, as shown in Equation (S6):

$$\mu(T, E) = \mu_{\infty} \exp\left[-\left(\frac{3\sigma_d}{5kT}\right)^2\right] \exp\left\{C \sqrt{\frac{eaE}{\sigma_d}} \left[\left(\frac{\sigma_d}{kT}\right)^2 - \Gamma\right]\right\} \quad (\text{S6})$$

Here, μ_{∞} is a temperature-independent mobility prefactor, as it is in the GDM, σ_d is the spatially correlated energetic disorder of the CDGM, C is an empirical constant (0.78) [8], e is an exponent, a is the hopping distance according to the CDGM, Γ is the positional disorder according to the CDGM. The slope and intercept yield the energetic disorder σ_d and the

mobility prefactor μ_∞ of the CGDM in the $\mu(T, 0)$ versus $(1000/T^2)$ plot, as shown in Figure S7c. The plot of the Poole-Frenkel factor β against $(1/kT)^{3/2}$ shows an extraction of the positional disorder Γ and hopping distance a according to CGDM by using the intercept and slope, as shown in Figure S7d. The parameters obtained using the CGDM are summarized in Table S1. The trend of the spatially correlated energetic disorder σ_d is similar to that of the uncorrelated energetic disorder σ . The result strongly implies a negative influence on the electrical properties of the high deposition rate. The positional disorder Γ decreased with a decrease of the deposition rate. Because the TAPC is naturally amorphous, the influence of the deposition rate on Γ is attributed to the different molecular-staking conditions during the thin-film formation. The calculated hopping distance of the TAPC clusters for various deposition rates was reduced from 0.39 and 0.29 to 0.22 nm. These results support our inference of the aforementioned possible molecular stacking; at a low deposition rate, the TAPC molecules can travel a long distance to find their lowest energy states to form the thin film; a high deposition rate hinders this process because of the rapidly upcoming layer deposition. Therefore, a low deposition rate enhances the possibility of molecular aggregation and, hence, an increase in the hopping distance.

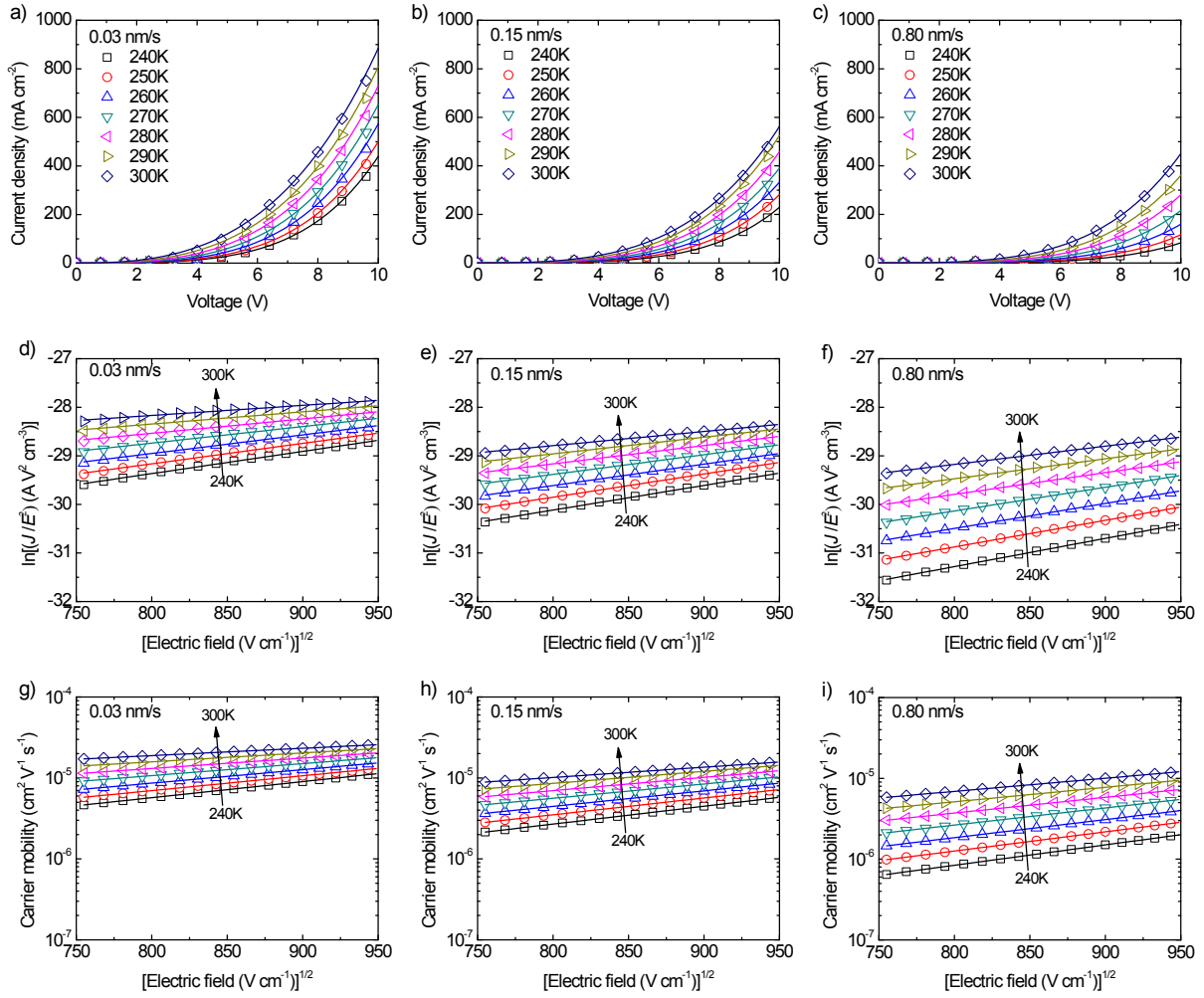


Figure S6. a-c) Variation of the SCLCs of the TAPC deposited at various deposition rates with varied temperatures for estimating the carrier mobility μ . The open symbols and solid lines indicate the experimental results and corresponding fits to the SCLC model. d-f) Plot of $\ln(J/E^2)$ of the TAPC deposited at various deposition rates against the square root of the electric field with varied temperatures for estimating the Poole-Frenkel factor β . g-i) Plot of the carrier mobility of the TAPC deposited at various deposition rates against the square root of the electric field with varied temperatures for estimating the zero-field mobility μ_0 .

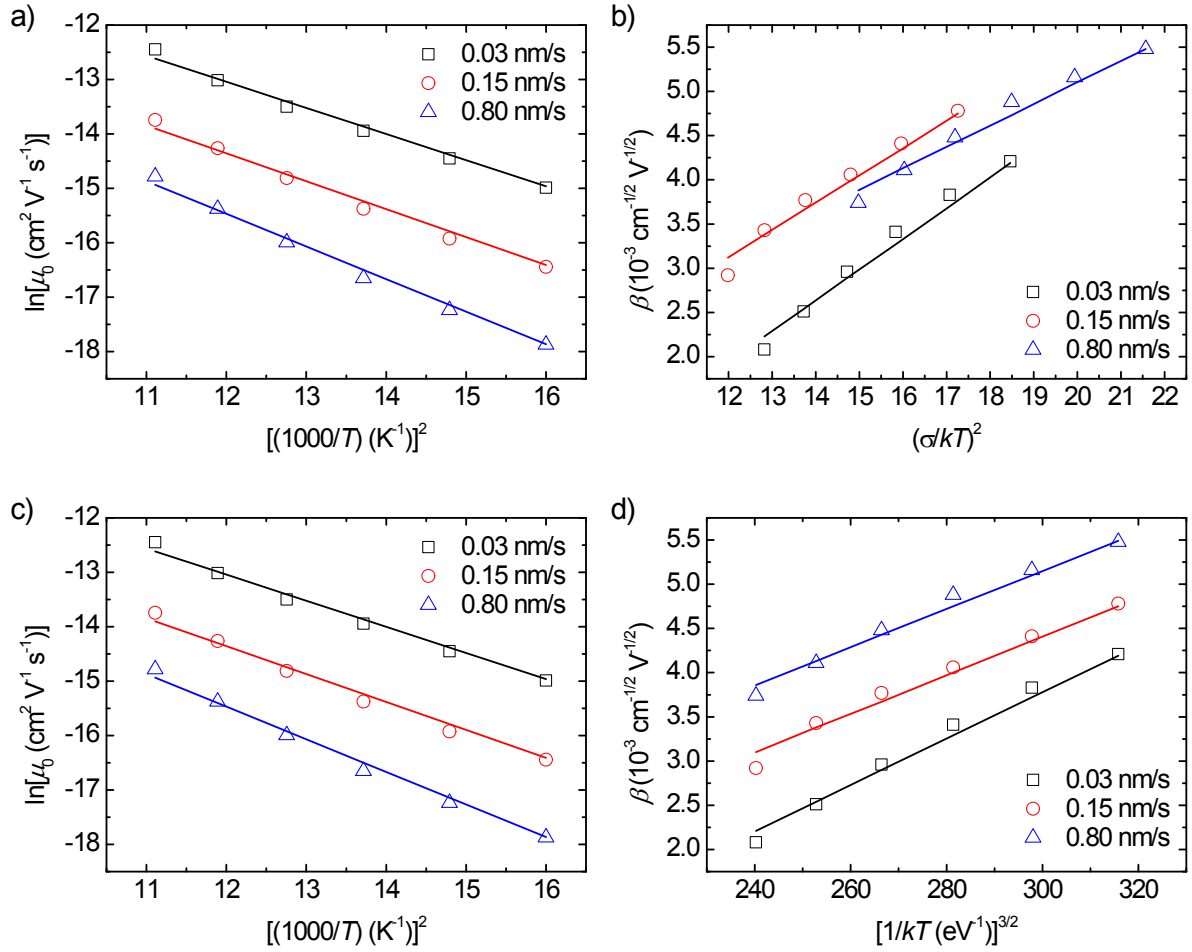


Figure S7. a) Zero-field mobility μ_0 of the TAPC deposited at various deposition rates as a function of $(1000/T)^2$ for extracting the energetic disorder σ and mobility prefactor μ_∞ of the GDM. b) Plot of the Poole-Frenkel factor β against $(\sigma/kT)^2$ for extracting the constant C_0 and positional disorder Σ^2 of the GDM. c) Zero-field mobility μ_0 of the TAPC deposited at various deposition rates as a function of $(1000/T)^2$ for extracting the spatially correlated energetic disorder σ_d and mobility prefactor μ_∞ according to the CGDM. d) Plot of the Poole-Frenkel factor β against $(1/kT)^{3/2}$ for extracting positional disorder Γ and hopping distance a according to the CGDM.

Table S1. Summary of the extracted parameters of the GDM and CDGM for the TAPC deposited at various deposition rates

Device	μ_{∞} (cm ² V ⁻¹ s ⁻¹)	σ (eV)	C_0 (cm ⁻¹ V ⁻¹)	Σ^2	σ_d (eV)	Γ	a (nm)
0.03 nm/s	1.00 x 10 ⁻³	0.090	3.46 x 10 ⁻⁴	6.4	0.100	5.1	0.39
0.15 nm/s	5.86 x 10 ⁻⁴	0.093	3.08 x 10 ⁻⁴	1.9	0.103	3.1	0.29
0.80 nm/s	2.53 x 10 ⁻⁴	0.100	2.43 x 10 ⁻⁴	-1.0	0.111	2.2	0.22

S9. Temperature-Dependent J_{SC} Measurement

The temperature-dependent J_{SC} can be expressed in Equation (S7) [9, 10]:

$$J_{SC}(T) = J_0 \exp\left(\frac{-\Delta}{kT}\right) \quad (S7)$$

Here, J_0 is a prefactor relating to the photogenerated carrier density, carrier mobility, and electric field, and Δ is the trap depth with respect to the corresponding band. Figure S8 shows the experimental results and fits to Equation (S7). The trap depth Δ increased when the deposition rate of the TAPC was increased. Although the hopping distance of carriers decreased when the deposition rate was increased, the deeper traps may compensate the ease of carrier hopping and reduce the electrical properties of the OPV devices with the TAPC deposited at a higher rate.

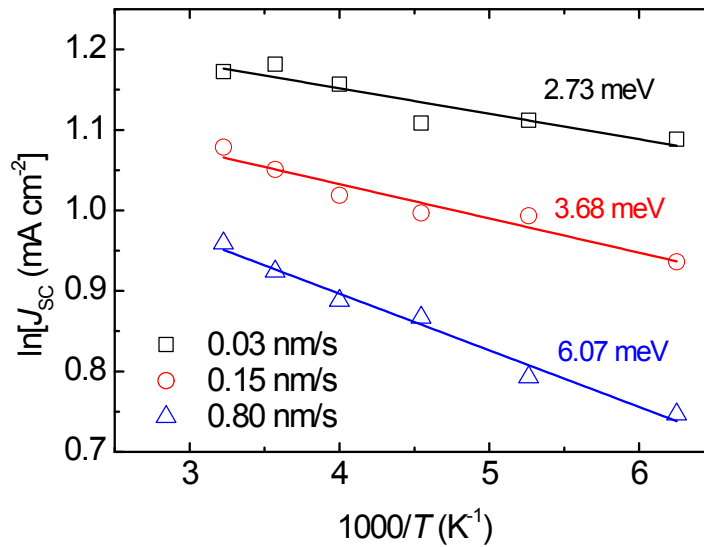


Figure S8. Plot of $\ln(J_{SC})$ against $(1000/T)$ for investigating the trap depth for the OPV devices with various deposition rates of the TAPC.

S10. Calculation of the J_S according to the Generalized Diode Equation

Although the intrinsic properties between inorganic and organic semiconductors considerably differ, OPV devices exhibit a behavior of rectification similar to that of their inorganic counterparts. Therefore, the J - V characteristics of the OPV devices can be simulated by Equation (1). Recall Equation (1) as Equation (S8) [11]:

$$J = \frac{1}{1 + R_S/R_{SH}} \left\{ J_S \left[\exp\left(\frac{V - JR_S A}{nkT/q}\right) - 1 \right] - \left(J_{PH} - \frac{V}{R_{SH} A} \right) \right\} \quad (S8)$$

Here, R_S and R_{SH} are the series and shunt resistances in a unit of Ω , respectively, J_S is the dark saturation current, A is the device active area, n is the ideality factor of a diode, k is the Boltzmann constant, T is the temperature, q is the elementary charge, and J_{PH} is the photocurrent. In general, the current of a diode exhibited a saturating trend and increased abruptly under a reverse and forward bias, respectively. However, the OPV devices typically exhibited a monotonically increased reverse current and a gradually increased forward current under a small forward bias [12, 13]. These phenomena were probably due to the trap-rich nature of organic materials. The monotonically increased reverse current may have been caused by a leakage current via the carrier hopping through the traps. This inference is supported by the experimental results, which showed voltage-dependent enhancements of the reverse currents. Therefore, in the current study, we considered the influence of the traps on the J - V characteristics by introducing a modified R_{SH} , which is dependent to the bias voltage. We propose that the R_{SH} can be expressed as $R_{SH0} \pm \beta V R_{SH0}$, where β represents the trap dependence, and the sign depends on the polarity of the bias voltage [14]. Figure S8a-c shows the fitting results for the OPV devices with the TAPC deposited at 0.03, 0.15, and 0.80 nm/s, respectively. Because of the modified model, all the reverse currents were perfectly consistent to the fitting according to Equation (S8). Although the currents under a small positive bias failed to be consistent with the fits, the linear plots presented a satisfactory agreement with the fits. The failed parts are attributable to the traps at either the anode or the cathode interfaces,

which enhance the thermally activated injection currents through the interface traps. Therefore, an in-depth understanding of the interface traps should be considered in future studies.

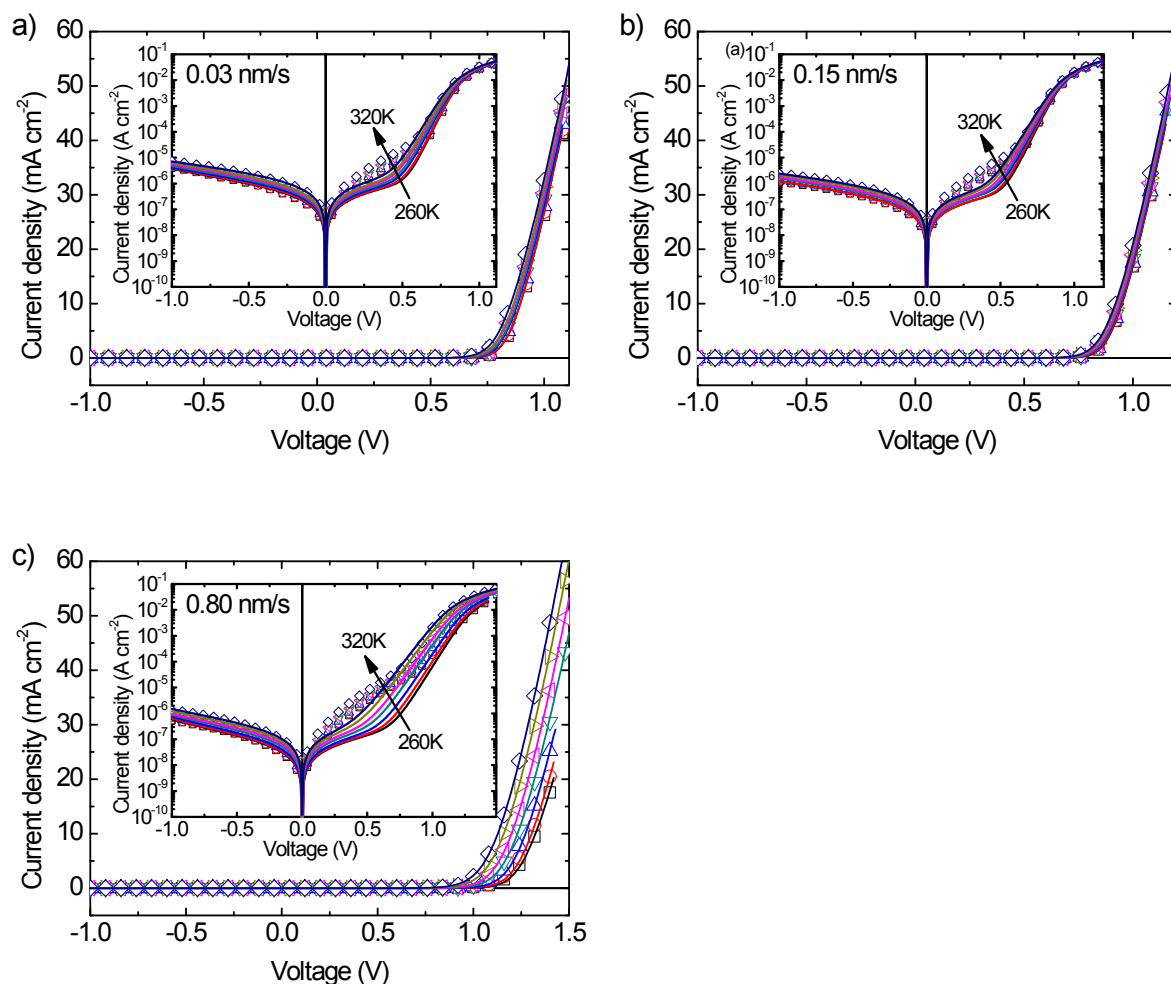


Figure S9. Experimental dark J - V characteristics and the fits to Equation (S8) at various temperatures for the OPV devices with the TAPC deposited at a) 0.03, b), 0.15, and c) 0.80 nm/s. The insets are the J - V characteristics plotted in semi-logarithmic scales. The open symbols and solid lines represent the experimental results and corresponding fits.

S11. Built-In Potential of the OPV Devices Estimated using the Mott-Schottky Relation

The Mott-Schottky relation describes a band bending in a junction formed by semiconductors as shown in Equation (S9) [15, 16]:

$$C^{-2} = \frac{2(V_{\text{bi}} - V)}{A^2 q \epsilon_r \epsilon_0 N} \quad (\text{S9})$$

Here, V_{bi} is the built-in potential, V is the bias voltage, A is the active area of the device, ϵ_r and ϵ_0 are the relative dielectric constant and the permittivity of the free space, respectively, q is the elementary charge, and N is the doping concentration. As shown in Figure S10, the experimental C - V results exhibited a straight line over a certain degree of bias voltage, which enabled estimating the V_{bi} to be 0.56, 0.61, and 0.78 V for the OPV devices with the TAPC deposited at 0.03, 0.15, and 0.80 nm/s.

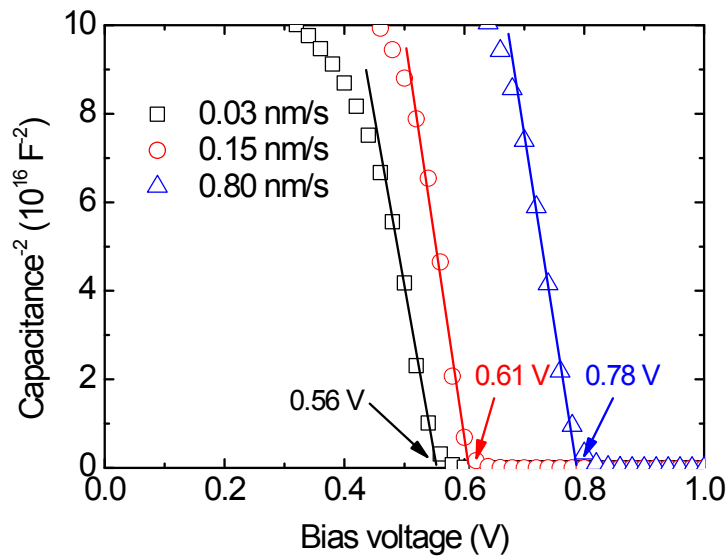


Figure S10. C - V characteristics of the OPV devices with the TAPC deposited at various deposition rates. The open symbols and solid lines denote the experimental results and corresponding fits to extract the V_{bi} . The arrows with texts indicate the value of the V_{bi} .

S12. Device Pattern and Encapsulation

The home-designed layout enabled fabricating five devices on one substrate. The organic layers were surrounded by a UV-curable epoxy resin (Everwide EXC345), applied using a syringe, followed by the coverage of a getter-attached glass that fitted the area of the epoxy resin. By softly pressing the cover glass, the epoxy resin became compact and prevented leaks. The encapsulation process was completed by exposing the epoxy resin to UV illumination.

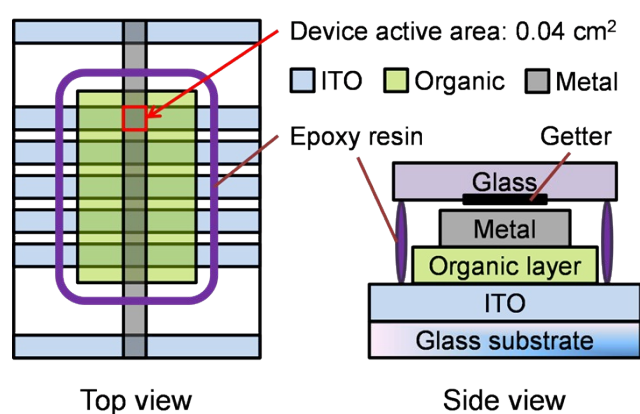


Figure S11. Illustrations of the device pattern and encapsulation from a top and side view

References

- [1] B. Pellissier, Photoelectron spectrometer, manufactured by Riken Keiki, in.
- [2] M. Uda, A. Nakamura, T. Yamamoto, Y. Fujimoto, Work function of polycrystalline Ag, Au and Al, *J. Electron Spectrosc. Relat.* 88 (1998) 643-648.
- [3] P.M. Borsenberger, L. Pautmeier, R. Richert, H. Bässler, Hole transport in 1,1-bis(di-4-tolylaminophenyl)cyclohexane, *J. Chem. Phys.* 94 (1991) 8276-8281.
- [4] R.H. Young, J.J. Fitzgerald, Dipole moments of hole-transporting materials and their influence on hole mobility in molecularly doped polymers, *J. Phys. Chem.* 99 (1995) 4230-4240.
- [5] T.-Y. Chu, O.-K. Song, Hole mobility of N,N'-bis(naphthalen-1-yl)-N,N'-bis(phenyl)-benzidine investigated by using space-charge-limited currents, *Appl. Phys. Lett.* 90 (2007) 203512.
- [6] M. Khan, W. Xu, Y. Bai, X. Jiang, Z. Zhang, W. Zhu, Electron mobility of 4,7-diphenyl-1,10-phenanthroline estimated by using space-charge-limited currents, *J. Appl. Phys.* 103 (2008) 014509.
- [7] H. Bässler, Charge transport in disordered organic photoconductors a Monte Carlo simulation study, *Phys. Status Solidi B* 175 (1993) 15-56.
- [8] S. Novikov, D. Dunlap, V. Kenkre, P. Parris, A. Vannikov, Essential role of correlations in governing charge transport in disordered organic materials, *Phys. Rev. Lett.* 81 (1998) 4472-4475.
- [9] I. Riedel, J. Parisi, V. Dyakonov, L. Lutsen, D. Vanderzande, J.C. Hummelen, Effect of temperature and illumination on the electrical characteristics of polymer-fullerene bulk-heterojunction solar cells, *Adv. Funct. Mater.* 14 (2004) 38-44.
- [10] H.-J. Song, J.Y. Kim, D. Lee, J. Song, Y. Ko, J. Kwak, C. Lee, Origin of the mixing ratio dependence of power conversion efficiency in bulk heterojunction organic solar cells with low donor concentration, *J. Nanosci. Nanotechnol.* 13 (2013) 7982-7987.

- [11] S. Yoo, B. Domercq, B. Kippelen, Intensity-dependent equivalent circuit parameters of organic solar cells based on pentacene and C₆₀, *J. Appl. Phys.* 97 (2005) 103706.
- [12] W.J. Potscavage Jr, S. Yoo, B. Kippelen, Origin of the open-circuit voltage in multilayer heterojunction organic solar cells, *Appl. Phys. Lett.* 93 (2008) 193308.
- [13] N.C. Giebink, G.P. Wiederrecht, M.R. Wasielewski, S.R. Forrest, Ideal diode equation for organic heterojunctions. I. Derivation and application, *Phys. Rev. B* 82 (2010) 155305.
- [14] C.-C. Lee, W.-C. Su, Y.-S. Shu, W.-C. Chang, B.-Y. Huang, Y.-Z. Lee, T.-H. Su, K.-T. Chen, S.-W. Liu, Decoupling the optical and electrical properties of subphthalocyanine/C₇₀ bi-layer organic photovoltaic devices: improved photocurrent while maintaining a high open-circuit voltage and fill factor, *RSC Adv.* 5 (2015) 5617-5626.
- [15] E. Meijer, A. Mangnus, B.-H. Huisman, D. de Leeuw, T. Klapwijk, Photoimpedance spectroscopy of poly(3-hexyl thiophene) metal-insulator-semiconductor diodes, *Synth. Met.* 142 (2004) 53-56.
- [16] G. Garcia-Belmonte, A. Munar, E.M. Barea, J. Bisquert, I. Ugarte, R. Pacios, Charge carrier mobility and lifetime of organic bulk heterojunctions analyzed by impedance spectroscopy, *Org. Electron.* 9 (2008) 847-851.